IEEE Access
Multidisciplinary | Rapid Review | Open Access Journal

Received January 8, 2020, accepted January 23, 2020, date of publication February 3, 2020, date of current version March 3, 2020.

Digital Object Identifier 10.1109/ACCESS.2020.2971221

Revealing the Mechanical Characteristics via Kinematic Wave Model for Snake-Like Robot Executing Exploration of Lunar Craters

XUYAN HOU[1], YUETIAN SHI[1], LONG LI[2], YE TIAN[3], YILIN SU[1], TIANXIANG DING[1], AND ZONGQUAN DENG[1]

[1]Aerospace Manufacturing Engineering Department, Harbin Institute of Technology, Harbin 150001, China
[2]School of Mechanical and Electrical Engineering and Automation, Shanghai University, Shanghai 200444, China
[3]Light Industry College, Harbin University of Commerce, Harbin 150028, China

Corresponding authors: Yuetian Shi (qthshiyuetian@163.com), Long Li (shangdalilong@163.com), and Ye Tian (tianyehuc@163.com)

This work was supported in part by the National Key Research and Development Program of China under Grant 2019YFB1309600, in part by the National Nature Science Foundation of China under Grant 51575123, in part by Self-Planned Task of the State Key Laboratory of Robot Technology and System (HIT) under Grant SKLRS201801B, in part by the Qian Xuesen Laboratory of Space Technology Seed Fund, and in part by the National Natural Science Foundation of China under Grant U1637207.

ABSTRACT It is extremely difficult to collect deep lunar soil samples during lunar exploration, as the average thickness of lunar soils is very large, and the power of lunar soil sampling systems is inherently limited. In this paper, we propose the use of serpentine robots to explore lunar craters. Our approach is to first design a kinematic wave model that allows the serpentine robot to satisfy all the requirements of lunar exploration. The resistance encountered by each part of the robot during its motions was measured to identify the parts with the greatest influence on each mode of locomotion to maximize its locomotive efficiency. Accordingly, we have designed a serpentine robot system based on the characteristics of snakes and constructed a kinematic model for serpentine robots in lunar crater environments. In addition, we constructed a lunar soil model using a discrete element method-multibody dynamics co-simulation platform, thus optimizing the locomotion strategy of the robot. The EDEM-ADAMS co-simulation platform was used to simulate the motions of the serpentine robot in a lunar crater, which yielded the resistance, speed of motion, and displacement of the robot's modules during its motions. The optimization analysis of the motion and environmental parameters of the serpentine robot included three variables: the inclination of the lunar crater's walls, the crawling angle of the robot, and the amplitude of the robot's kinematic wave. The dependence of the motions of the serpentine robot on these variables was analyzed using maximum and averaged force values. Finally, validation experiments were performed using a serpentine robot model. Thus, we have optimized the locomotion strategy of the serpentine robot for lunar craters.

INDEX TERMS Serpentine robot, lunar soil particles, lunar crater walls, discrete element theory, motion optimization.

I. INTRODUCTION

Lunar craters are ring-shaped pits formed by meteorite impacts, and the Moon's geological profile is reflected by the profile of these craters [1]. Therefore, drilling from the side of a lunar crater's walls will greatly reduce the drilling distance required to collect deep lunar soil samples [2]. In addition, the walls of these lunar craters contain soils that span a wide range of ages at each level of depth. Hence, a geological study on the walls of lunar craters will greatly enhance our understanding of the Moon's structure. Hence, it may be said that the development of robotic technologies for the investigation of lunar crater walls is of utmost importance for the realization of humankind's scientific goals regarding lunar exploration [3].

Various robots have been used to explore the Moon's surface. The first of these robots used wheels for locomotion. Wheels consume little energy and allow the robot to move

The associate editor coordinating the review of this manuscript and approving it for publication was Chenguang Yang.

quickly and efficiently, but they can only be used in certain parts of the lunar environment where the surface is flat and hard [4]–[7]. Tracked lunar rovers were developed based on tank tracks to deal with the unevenness of the lunar surface, but these robots could not move in a flexible manner. This has prompted researchers to search for new forms of locomotion [8].

As this research continues to progress, researchers have become increasingly interested in solutions from the natural world, which has resulted in the advent of bionic robots [9]–[12]. The first types of these robots were legged robots, which are also the most diverse category of bionic robots. The first bionic robots were quadrupeds, which were promptly followed by biped robots [13], and then hexapods and many-legged robots. The way legged robots mimic the way animals move improves their ability to adapt to different environments [14], [15]. However, these robots tend to have a high center of gravity, which makes them unstable. These robots also require highly controlled environments to function optimally, and they do not work well on loose surfaces [16]. Hence, legged robots cannot fully satisfy the requirements of lunar exploration. As a part of efforts to develop a new mode of robotic motion, researchers have now diverted their attention to snakes, and bionic robots are now being developed to move without limbs [17]–[19].

This development is also applicable to lunar exploration robots and vehicles. Wheeled robots, which are the most common type of robot, have evolved into tracked robots that are capable of surmounting various obstacles. The next step was the development of legged robots and landing gear, which can adapt to an even greater variety of terrains [20]–[22]. In the face of increasingly complex terrains and demanding environments, serpentine robots have now become an attractive option for planetary and lunar exploration [23].

This study is inspired by the unique crawling gait of snake species in desert terrains [24]–[26]. For the development of serpentine robots, we studied the structural features and gait of snakes in the natural world to model their movements in lunar craters [27]. In addition, mathematical and physical models were used to calculate the geometric angles, driving force, and structures that would maximize the efficiency of a snake moving in sand. The research map of this study is shown in Fig. 1. In summary, we chose a serpentine model to address the issues facing lunar crater exploration. We then constructed a lunar soil model and modeled the motion of serpentine robots in lunar craters to establish their patterns of motion. Experiments were then performed to validate our theoretical findings.

The parameters of the prototype experiment were derived from the simulation analysis. The motions of the prototype robot were then observed, and the differences between the experiment and simulation analysis were analyzed. During lunar exploration, the robot will encounter situations where it must avoid an obstacle or move to a fixed location, which requires the robot to move according to specific kinematic waveforms. In this work, these specific kinematic waveforms are denoted as the "kinematic wave model." Our approach is to first design a kinematic wave model that allows the serpentine robot to satisfy all the requirements of lunar exploration. The resistance encountered by each part of the robot during its motions was measured to identify the parts with the greatest influence on each mode of locomotion to maximize its locomotive efficiency. Although the abovementioned quantities are difficult to measure in real (physical) experiments, a simulation analysis will reveal the underlying patterns of these quantities.

II. MODELING THE CRAWLING GAIT OF THE KINEMATIC-WAVE-MODEL-BASED SERPENTINE ROBOT

A simulation analysis was performed on the motions of a serpentine robot by conducting EDEM-ADAMS co-simulations, where the robot was made to move in specific wave-like motions based on the movements of snakes. The crawling motions of the serpentine robot were then kinematically modeled to construct the kinematic wave model.

The most common type of snake gait was used to validate the methods of this study. If the amplitude, frequency, and phase of the crawling motion are different, the trajectory curve taken by the serpentine robot will change. The curvature equation proposed by Hirose et al. for the motions of a serpentine curve in one cycle may be expressed as

$$\rho(s_p) = \frac{-2K_n\pi\alpha_0}{L}\sin(\frac{2K_n\pi s_p}{L}). \tag{1}$$

After the motions are converted to Cartesian coordinates, and the serpentine body is decomposed into n segments, one obtain the definition of angle function adjacent links of moving serpentine robot:

In the coordinate system, the angle function of the serpentine robot may be expressed as

$$\theta_i' = \alpha' \cos\left(\omega + \left(i + \frac{1}{2}\right)\beta'\right) + i\gamma \tag{2}$$

The surface friction of the serpentine robot was theoretically modeled using an anisotropic viscous friction model, based on the environment of meteorite craters. By simplifying the angular relations of the robot, the following surface friction model was obtained for each segment of the robot:

$$\begin{aligned} F_{R,x,i} &= c_t\,\dot{x}_i + (c_t - c_n)\frac{y_{i+1} - y_{i-1}}{2l}\,\dot{y}_i + G\sin\eta/\cos\theta \\ F_{R,y,i} &= (c_t - c_n)\frac{y_{i+1} - y_{i-1}}{2l}\,\dot{x}_i + c_n\,\dot{y}_i + G\sin\eta/\sin\theta \end{aligned} \tag{3}$$

As lunar soils are very loose, a part of the serpentine robot will sink into the lunar surface when it is moving on the Moon. Therefore, it is necessary to account for stresses from the lunar soil on the robot. The behavior of soft, deformable surfaces was modeled using Bekker's pressure-sinkage and shear stress equations.

Based on decades of lunar exploration data, it is known that a lunar rover will sink to some extent (5–15 mm) in lunar soil, due to the looseness of these soils. Although the serpentine

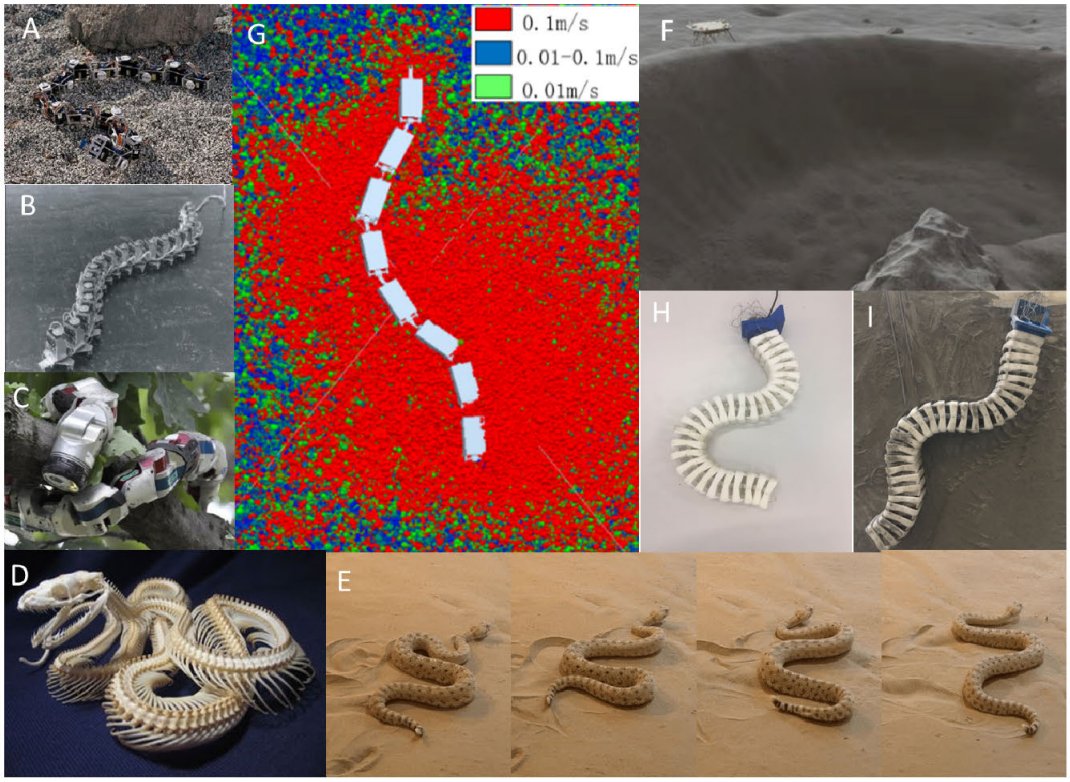

FIGURE 1. Serpentine robots have long been used in the aerospace field, such as (A) NASA's serpentine robots [28] for space exploration. Figure (B) is the earliest snake-like robot [29] , and Figure (C) is a snake tree-climbing robot at Carnegie Mellon University [30]. (D) The snake has a unique bone structure and a high degree of freedom of movement, and (E) can climb hills in the desert. (F) In the working environment of the lunar crater, the serpentine robot can do the work that other robots cannot. (G) The research method of stipulating the robot's motion trajectory to study the force state is used to create the lunar soil environment for dynamics research. Finally, (F) the 3D printed model was used to (F) verify the law under the simulated lunar soil.

robot will sink less in the lunar soil, the effects of sinkage on the normal and tangential stresses of the robot must be considered.

The lateral friction of the robot against lunar soils is given by

$$f_c = Wk(k_c/d + k_\varphi)z^n + W(c + \sigma \tan\varphi)(1 - e^{-j/J}). \quad (4)$$

The frontal friction caused by the inclination of the crater's walls may be obtained by multiplying friction with the inclination coefficient, k_d.

$$F_t = bk_d W_d(k_c/b + k_\varphi)z^n \quad (5)$$

An expression for the forces applied by lunar soil on the serpentine robot in the global t–n coordinate system may then be obtained via a coordinate system conversion. The theoretical model that represents all the forces acting on the serpentine robot in a lunar crater is (6), as shown at the bottom of the next page.

c_t—Tangential viscous friction coefficient, c_n—Normal viscous friction coefficient, k_c—Cohesive soil deformation modulus, d—Bottom length, b—Bottom width, z—Deformation depth, k_φ—Soil deformation modulus due to internal friction, n—Soil deformation index, j—Shear deformation, J—Modulus of horizontal shear deformation, k—Coefficient of friction between soil and objects, W—Lateral subsidence, W_d—Front subsidence, k_d—Tilt factor.

III. SIMULATING THE MOTIONAL CHARACTERISTICS OF THE SERPENTINE ROBOT VIA EDEM-ADAMS CO-SIMULATIONS

The soil environment of lunar craters is complex, as it contains lunar soil, rocks, and irregular soil particles that vary in shape and size. The finite element method would not be able to model the minute variations of the crater's soil surface structures, nor the actions of the various lunar soil particles on the serpentine robot. Therefore, the discrete element method was used to model the soils of lunar craters.

Simulated lunar soils from the School of Astronautics of the Harbin Institute of Technology were used to determine the attributes and parameters of the lunar soil to validate the accuracy and precision of the simulation analysis. Here, we have incorporated the concept of the fractal dimension to model irregular lunar soil particles. The distributions of the granule circumferences and areas of the simulated lunar soil were measured, and the fractal dimension of the simulated lunar soil was adjudged on this basis. It was thus determined

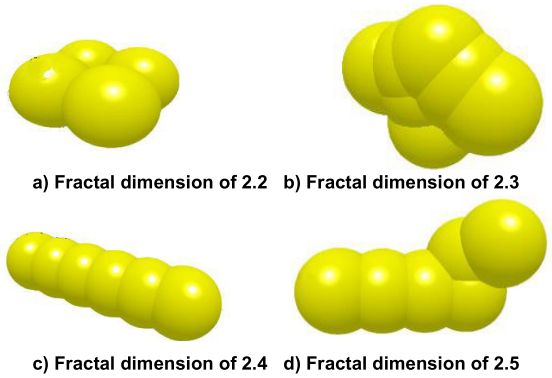

FIGURE 2. Discrete particle models for lunar soils.

TABLE 1. Parameters of the simulated lunar soils.

Parameter of the simulated lunar soil	Value
Modulus of deformation due to pressure, Kn (Pa/m)	1.4×10^6
Sinkage index, n	1.125
Cohesion, c(Pa)	179.71
Internal friction, φ(0)	32.050
Soil shear deformation modulus, K (mm)	10.2
Poisson's ratio	0.3
Shear modulus (Pa)	1×10^8
Density (kg/m^3)	2500
Surface energy (J)	6000

that the simulated lunar soils have fractal dimensions between 2.2 and 2.5. Finally, a set of discrete particle models was constructed for each type of lunar soil, according to the fractal dimensions of their particles, as shown in Fig. 2.

The parameters of the discrete particle model for each type of lunar soil were defined according to the macroscopic properties and material attributes of the simulated lunar soils. These parameters are shown in Table 1.

Boolean addition was used to create five particle models, which were used to perform discrete element simulations

TABLE 2. Distribution of particle radii in the simulated lunar soils.

Type of soil	Maximum length (mm)
Rock particles	2
Lunar soil particles (with a fractal dimension of 2.2)	0.316
Lunar soil particles (with a fractal dimension of 2.3)	0.462
Lunar soil particles (with a fractal dimension of 2.4)	0.474
Lunar soil particles (with a fractal dimension of 2.5)	0.403
Lunar soil particles (with a fractal dimension of 2.6)	0.524

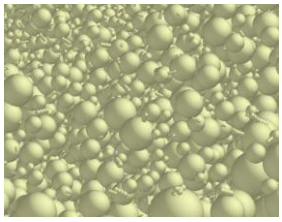

FIGURE 3. Radii distributions of simulated lunar soils with different shapes.

of the soil environment in lunar craters. The large particles represent rock particles, whereas the small, irregular particles represent soil particles. Large rocks that may act as environmental obstructions were excluded from this model. The simulation analysis was performed in EDEM by inputting the five particles in a 1:1:1:1:1 ratio to generate a set of simulated lunar soils randomly (see Fig. 3). The maximum particle sizes of these soils are shown in Table 2.

The initial lunar soil samples deposited on the lunar crater's walls must be made to be static in EDEM to simulate the windless environment of lunar craters. However, the particles will collide with and compress each other as they move, and they will also move at a certain speed during this process.

$$
\begin{aligned}
\mathrm{F}_t &= \sum_{i=1}^{N} \left\{ \begin{array}{l} \cos\theta_i \left[c_t \dot{t}_i + (c_t - c_n) \dfrac{n_{i+1} - n_{i-1}}{2l} \dot{n}_i \right] + G \sin\eta \\ + \sin\theta_i \left[(c_t - c_n) \dfrac{n_{i+1} - n_{i-1}}{2l} \dot{t}_i + c_n \dot{n}_i \right] + G \cos\eta \\ + 2\cos\theta_i \left[Wk(k_c/d + k_\varphi) z^n + W(c + \sigma \tan\varphi)(1 - e^{-j/J}) \right] \\ + bk_d W_d (k_c/b + k_\varphi) z^n \cos^2\theta_i \end{array} \right\} \\
\mathrm{F}_n &= \sum_{i=1}^{N} \left\{ \begin{array}{l} \sin\theta_i \left[c_t \dot{t}_i + (c_t - c_n) \dfrac{n_{i+1} - n_{i-1}}{2l} \dot{n}_i \right] + G \sin\eta \tan\theta_i \\ + \cos\theta_i \left[(c_t - c_n) \dfrac{n_{i+1} - n_{i-1}}{2l} \dot{t}_i + c_n \dot{n}_i \right] + G \cos\eta \cot\theta_i \\ + 2\sin\theta_i \left[Wk(k_c/d + k_\varphi) z^n + W(c + \sigma \tan\varphi)(1 - e^{-j/J}) \right] \\ + bk_d W_d (k_c/b + k_\varphi) z^n \sin\theta_i \cos\theta_i \end{array} \right\}
\end{aligned} \tag{6}
$$

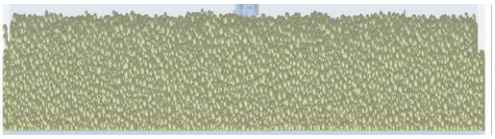

FIGURE 4. Generation of soil particles in the initial state.

Therefore, the method shown in Fig. 4 was used to stack the particles. The model was randomly filled with particles, which were allowed to fall freely. The particle generation process was then stopped, and the process was terminated. Thus, stratified layers of static particles were produced, and a sufficient number of particles were generated to attain the predetermined soil thickness.

A simplified 3D model of the serpentine robot was constructed, which does not include the small components that link the segments, or the electric motor and transmission devices. This model accounts for the degrees of freedom of each joint and the mode of locomotion of the serpentine robot in lunar soils. Furthermore, the model is fully sealed against dust.

The serpentine robot consists of eight modules, and each module may be subdivided into a body and steering joint. The motions of the robot are driven by drivers at each joint. The usable area at the rear of each module was reduced to prevent inter-module collisions to maximize the range of rotation of each joint. Continuous joints were used in the robot, and any joint can be locked into an orthogonal angle (or some other configuration) with the next joint to maximize the flexibility of the simulation. The modules were designed as sealed boxes to prevent intrusion by lunar dust particles, thus ensuring that the robot is sealed against dust.

After the types, positions, and numbers of the joints were defined in ADAMS, each joint was then controlled. Based on the kinematic wave model for serpentine robots (Equation 2-2), the horizontal steering functions of the seven joints can be defined as follows:

$$\begin{aligned}
\theta_{h,1} &= (pi/6)^{*}SIN(pi^{*}time) \\
\theta_{h,2} &= (pi/6)^{*}SIN(pi^{*}time + pi/2) \\
\theta_{h,3} &= (pi/6)^{*}SIN(pi^{*}time + 5^{*}pi/6) \\
\theta_{h,4} &= (pi/6)^{*}SIN(pi^{*}time + 7^{*}pi/6) \\
\theta_{h,5} &= (pi/6)^{*}SIN(pi^{*}time + 9^{*}pi/6) \\
\theta_{h,6} &= (pi/6)^{*}SIN(pi^{*}time + 11^{*}pi/6) \\
\theta_{h,7} &= (pi/6)^{*}SIN(pi^{*}time + 13^{*}pi/6) \qquad (7)
\end{aligned}$$

The parameters of the serpentine robot under these steering functions are as follows: The mass, length, and width of each module are 1.0189 kg, 200 m, and 100 mm, respectively, and the kinematic wave amplitude of the serpentine robot is $\alpha = \pi/6$. Fig. 5 shows the simulated motions of the serpentine robot from 0–1.5 s when the angle between the robot's direction of advancement and inclination (henceforth referred to as the advancement-inclination angle) is 0° and the rotational angle of the robot is $\gamma = 0°$.

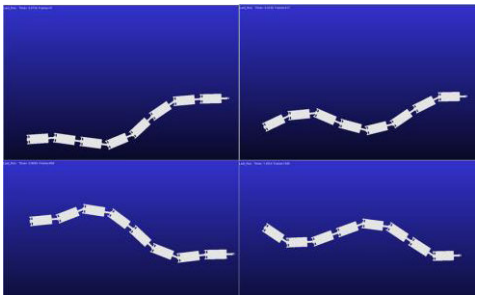

FIGURE 5. ADAMS-simulated motions of the snake robot from 0 s to 1.5 s.

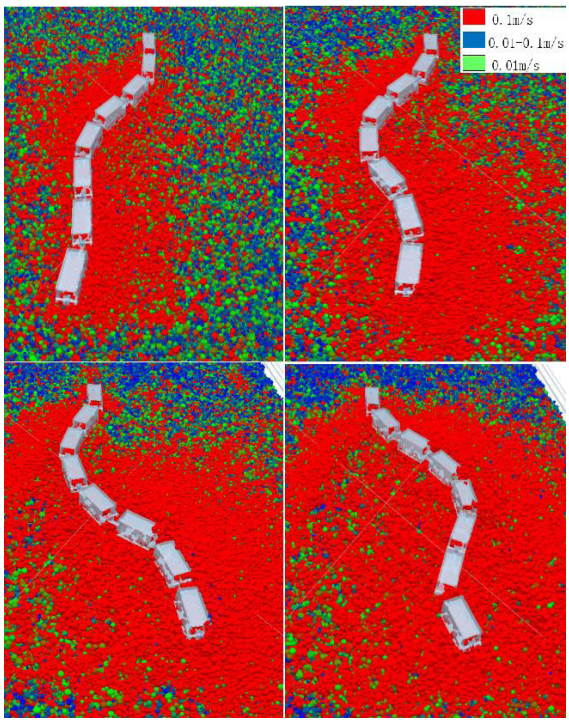

FIGURE 6. EDEM-ADAMS co-simulation.

After the EDEM-ADAMS co-simulation platform was constructed, the EALink add-on was used to facilitate data transfer between EDEM and ADAMS. EALink enables bidirectionally-coupled computations between EDEM and ADAMS, and the ADAMS-simulated motions of the serpentine robot were thus obtained, as shown in Fig. 6.

It may be observed that the serpentine robot is lying on the surface of the lunar soil layers, and that the bottom of the robot is parallel to the lunar soil's surface. The processes of the coupled simulation are illustrated in Fig. 6b. Here, it is shown that the soil particles will be continuously stacked along the sides of the serpentine robot due to the angle of inclination of the surface. Hence, the serpentine robot must overcome very large soil friction forces to move in lunar craters.

The parameters selected for this simulation experiment are as follows: a lunar crater inclination of 45°, kinematic wave amplitude of $\alpha = \pi/6$, and an advancement-inclination angle of 0°. At the end of the simulation, the X and Y forces that

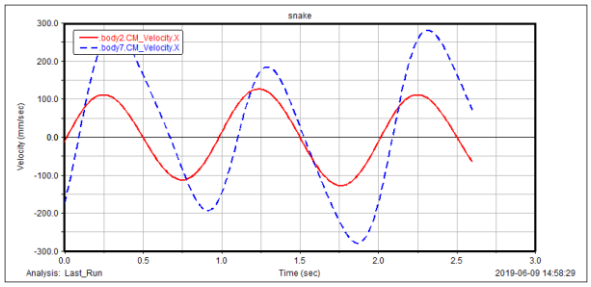

FIGURE 7. Velocity curves of the two modules of the serpentine robot.

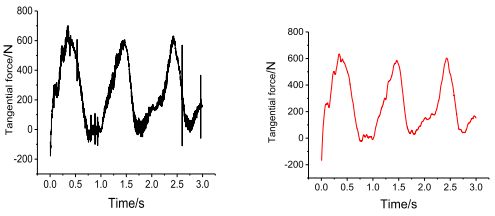

FIGURE 8. Smoothed force curve.

acted on each module were plotted and compared with the theoretical model.

As the soil particles are highly diverse, irregular in shape, and countless in number, the computational workload in these simulations is extremely large. The movements of the serpentine robots must be significant in a short period of time to ensure that the simulations can be completed in a reasonable amount of time. Therefore, the periodicity of the motions of the serpentine robot was set to 2 s. The velocity curves of the two modules of the serpentine robot are shown in Fig. 7.

The tangential force curve of the second module will be discussed below. The first 0.05 s of this curve were omitted from the figure, as they simply correspond to the period when the serpentine robot transitions from the ''imported'' state to the initial state. As the particles move in an irregular manner during the simulation, the force curves will exhibit fluctuations in certain parts of the curve. The curve produced by smoothing these fluctuations is shown in Fig. 8.

It is thus shown that the force acting on the module exhibits a periodic pattern. In the following section, we will analyze these patterns in detail by performing more simulations, and by collecting the force data of each module.

IV. OPTIMIZING THE CONTROL STRATEGY FOR SERPENTINE ROBOTS MOVING IN LUNAR CRATERS

The motions of a serpentine robot on the surface of a lunar crater will be affected by various factors, including the materials used to build the robot, its mode of locomotion, and its external environment. Any change to the mode of locomotion or motion of the serpentine robot will alter the amount of energy it consumes. Changes in the surface's angle of inclination and flatness will also alter the external forces acting on the serpentine robot. The lunar environment is very complex and there are very few instances where the walls of a lunar

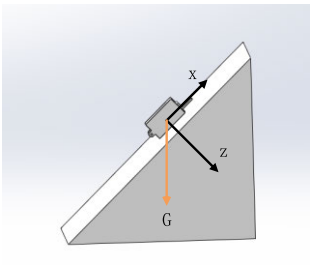

FIGURE 9. Simulated gravity values.

TABLE 3. X and Z gravitational components.

Inclination of the lunar crater's walls (°)	X component of gravity (m/s^2)	Z component of gravity (m/s^2)
45	-1.156	1.156
50	-1.259	1.05
55	-1.4159	0.8175
60	-1.3393	0.93779

crater have been explored. Consequently, it is impossible to confirm experimentally the conditions at which the serpentine robot will exhibit maximal efficiency and minimal energy use. Therefore, simulation analyses were performed to study locomotion and control strategies for a serpentine robot moving along the walls of a lunar crater. The optimization analysis was performed using three parameters: the inclination of the lunar crater's walls, and the robot's crawling angle and kinematic wave amplitude. Four scenarios were simulated for each parameter, and we processed approximately 40,000 datasets to obtain the force curves and maximum force of the six modules in each working scenario.

The parameters of the serpentine robot are as follows: The mass of the serpentine robot = 1.0189 kg; inclination of the crater wall = 45°; kinematic wave amplitude of the robot, $\alpha = \pi/6$; advancement-inclination angle = 0°. In this section, these parameters are the reference parameters, and the inclination of the crater's walls was treated as the controlled variable. Based on the lunar soil deposition model, the direction of gravity was varied to simulate different crater-wall inclinations; thus, we avoided having to rebuild the lunar soil deposition model for each crater-wall inclination. As shown in Fig. 9, the positive direction of the x-axis is the direction of advancement of the head of the serpentine robot in the initial state, and the positive direction of the z-axis is the direction that is downwards and perpendicular to the inclined plane. Gravity was defined as two components, and the angle of inclination was varied by altering the values of these components (see Table 3).

Fig. 11 illustrates the force diagrams of the serpentine robot under the reference parameters. The robot is divided into six modules: modules one and two are the front, modules three

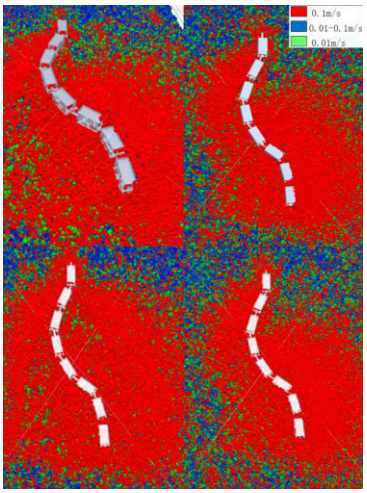

FIGURE 10. Simulation of different angles of inclination.

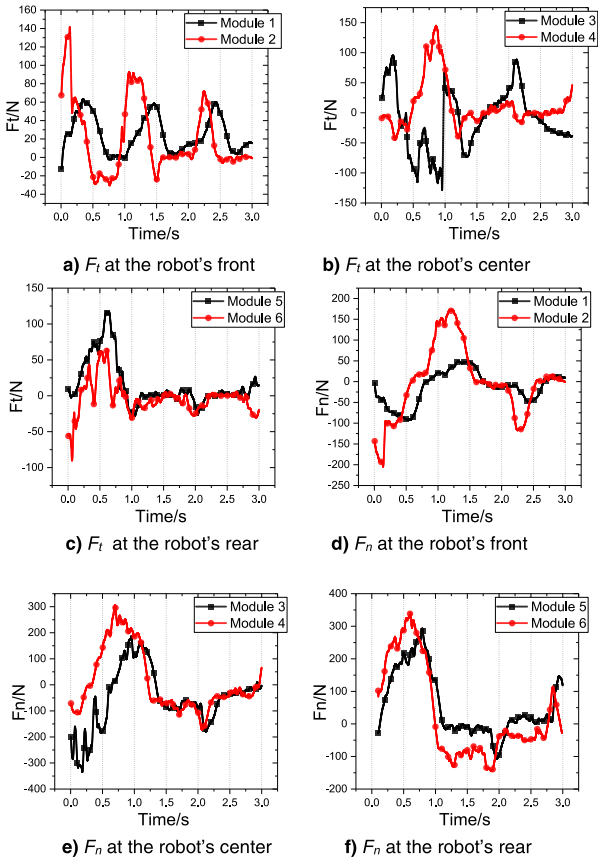

FIGURE 11. Force diagrams of the serpentine robot under the reference parameters.

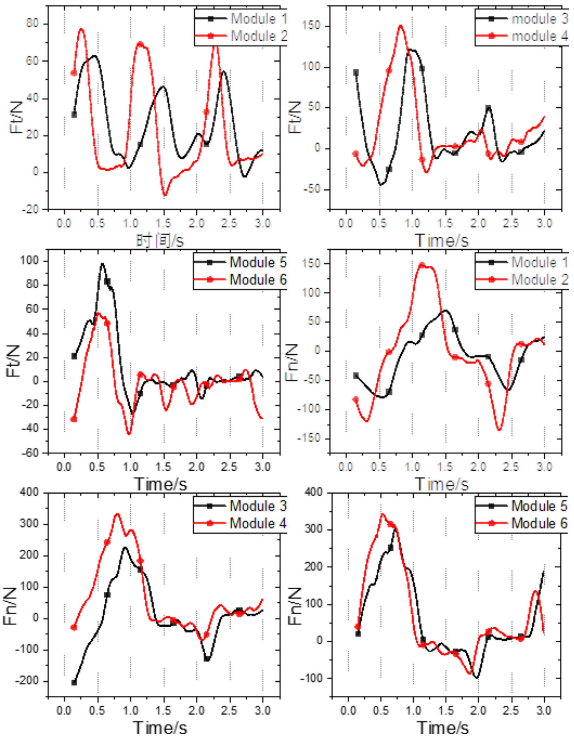

FIGURE 12. Force diagrams of the serpentine robot when the angle of inclination is 50°.

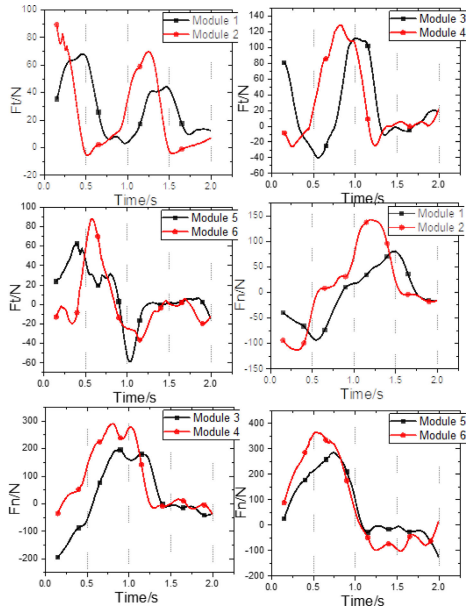

FIGURE 13. Force diagrams of the serpentine robot when the angle of inclination is 55°.

and four are the middle, and modules five and six are the rear. The tangential and normal forces are detected respectively.

Here, we altered one of the variables while keeping the other variables unchanged from the reference parameters. The force diagrams of the serpentine robot when the crater-wall's angle of inclination was 50° are shown in Fig. 12.

Based on the above data, the maximum (single module) tangential force (180.699 N at 0.645 s) occurs at the fourth module, whereas the maximum normal force occurs at the sixth module (341.66 N at 0.525 s). These forces gradually weakened after their respective maxima.

Fig. 13 shows the force diagrams of the serpentine robot when the angle of inclination is 55°.

Here, it is shown that the maximum tangential force (128.263 N at 0.765 s) occurs at the fourth module, whereas the maximum normal force occurs at the sixth module

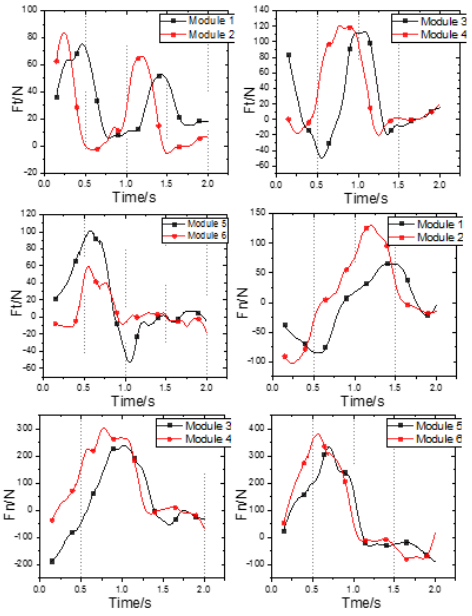

FIGURE 14. Force diagrams of the serpentine robot when the angle of inclination is 60°.

TABLE 4. Maximum force on a module at each angle of inclination.

Angle of inclination	45°	50°	55°	60°
Tangential force/N	145.1 04	180.6 99	128.2 63	120.1 79
Normal force/N	331.0 41	341.6 6	364.4 69	378.1 44

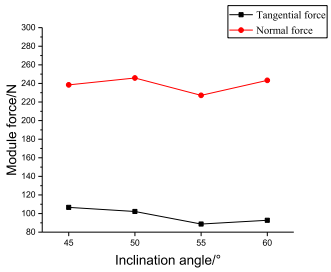

FIGURE 15. Average maximum force on the robot at the four different angles of inclination.

(364.469 N at 0.520 s). These forces then weakened after their respective maxima were reached.

Fig. 14 shows the force diagrams of the serpentine robot when the angle of inclination is 60°.

The data show that the maximum tangential force occurs at the fourth module (120.179 N at 0.780 s), and the tangential force on the second and third modules is slightly weaker than the maximum tangential force. The maximum normal force occurs at the sixth module (378.144 N at 0.615 s), and the maximum forces on the fourth and fifth modules both reached 300 N. All these forces gradually weakened after reaching their maxima.

The most important aspect of the effects of inclination on the serpentine robot is the degree by which the angle of inclination affects the robot. Here, we have performed simulations with crater-wall inclinations of 45°, 50°, 55°, and 60°. To reveal the degree by which the crater-wall's inclination affects the motions of the serpentine robot, we measured the tangential and normal forces experienced by each module and obtained the trends of these forces by processing the resulting data. We then calculated the peaks and periodicity of the friction experienced by the robot.

Thus, we calculated the maximum forces acting on the serpentine robot when it is moving on a lunar crater's walls. In particular, the direction of the tangential force is identical to the robot's direction of advancement and equivalent to the force provided by the driving system, which controls the advancement of the robot. The normal force is perpendicular to the robot's direction of advancement, and it controls the steering of the robot's modules and maintains its snake-like movement curve. In the data analysis, the signs only represent the direction of the force and are independent of magnitude. The driving force that should be possessed by the serpentine robot and its friction are forces of equal magnitude that act in opposing directions. Table 4 shows the maximum forces acting on the modules in each working scenario.

As the shape and movement of the particles are intrinsically irregular, the force maxima will show the maximum force that the serpentine robot must withstand, but they do not show the extent by which the motions of the robot are affected by environmental parameters or the robot's intrinsic parameters. Hence, the average values were used to analyze the effects of the experimental parameters and variables on the motional characteristics of the robot. Fig. 15 shows the averaged maximum force on the robot at each of the four angles of inclination.

After investigating the effects of the angle of inclination on the robot, we then examined how variations in the robot's crawling angle and kinematic wave amplitude affected the robot. For the sake of brevity, we will only show the findings derived from data analysis.

The crawling angle was varied while the other reference parameters were maintained unchanged. In this analysis, the direction along the oblique plane that maximizes the incrementation of vertical height is defined as the reference axis, and the crawling angle is 0° in this direction. The crawling angle is defined as the angle between the robot's direction of advancement and the reference axis. In this section, we analyzed scenarios where the crawling angle was 0°, 20°, 40°, and 60°. The simulation of each crawling angle is shown in Fig. 16.

As a very large amount of data was collected, the force diagrams of the serpentine robot are not shown here. Table 5 shows the maximum force on singular modules at each crawling angle.

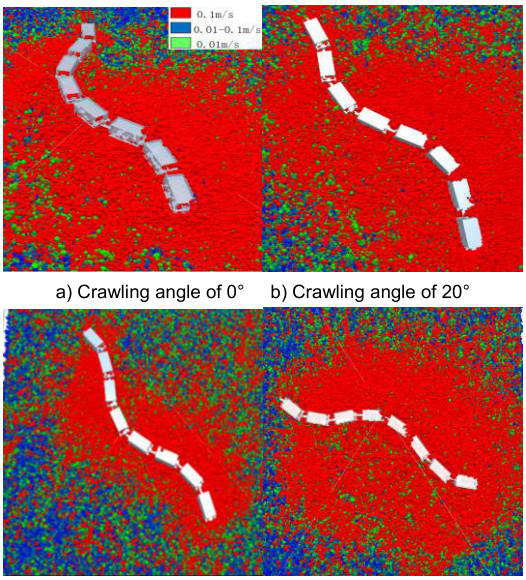

FIGURE 16. Simulation of different crawling angles.

TABLE 5. Maximum force on singular modules at each crawling angle.

Crawling angle	0°	20°	40°	60°
Tangential force/N	145.104	460.028	289.674	362.871
Normal force/N	331.041	494.836	300.517	238.202

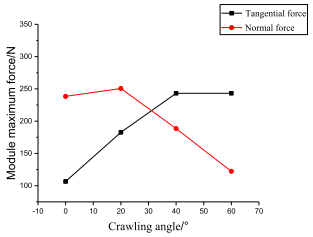

FIGURE 17. Average maximum force on the robot at the four different crawling angles.

In these scenarios, the maximum friction encountered in the tangential and normal directions was 460.028 N and 494.836 N, respectively.

We then processed the crawling angle dataset by excluding the maximum and minimum single-module forces, and thus obtained the maximum averaged force on the serpentine robot at each crawling angle (see Fig. 17).

By analyzing the changes in force that accompanied each stepwise increase in crawling angle, it was observed that the magnitude of the tangential force increased by 76.07 N (71.35% increase) when the crawling angle increased from 0° to 20°, and by further 60.46 N (33.1% increase) when the crawling angle increased from 20° to 40°. As the tangential force increased by 136.55 N with the increase in the crawling angle from 0° to 60°, the required maximum average tangential force increased by 22.75 N for each 10° increase in the crawling angle.

By analyzing the normal forces on the robot, it may be observed that the normal force increased by 18.23 N when the crawling angle increased from 0° to 20° and decreased by 128.07 N when the crawling angle increased from 20° to 40°. As the normal force decreased by 116.08 N with the increase in the crawling angle from 0° to 60°, the required maximum average normal force decreased by 19.35 N for each 10° increase in the crawling angle.

When a living snake crawls on steep sandy slopes, it will tend to use larger motions. Therefore, we chose the amplitude of the kinematic wave as the third variable of the optimization analysis. Here, we analyzed scenarios where α' was 30°, 40°, 50°, and 60°. The gait of the serpentine robot in each scenario is shown in Fig. 18. By obtaining the tangential and normal forces acting on each module, we may then obtain the changes in force at each point in time.

The previously described approach was used to analyze the effects of kinematic wave amplitude on the serpentine robot. Table 6 shows the maximum force on a single module at each kinematic wave amplitude.

In the four listed scenarios, the maximum friction in the tangential and normal directions was 304.682 N and 512.924 N, respectively.

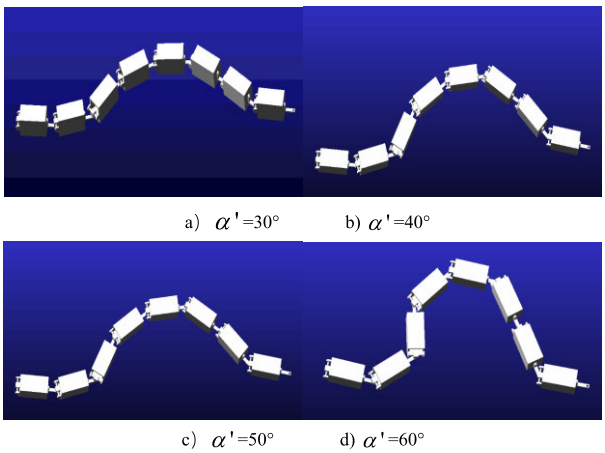

FIGURE 18. Gait of the serpentine robot at each kinematic wave amplitude.

TABLE 6. Maximum force on a single module at each kinematic wave amplitude.

Kinematic wave amplitude	30°	40°	50°	60°
Tangential force/N	145.104	173.940	181.660	304.682
Normal force/N	331.041	507.022	320.391	512.924

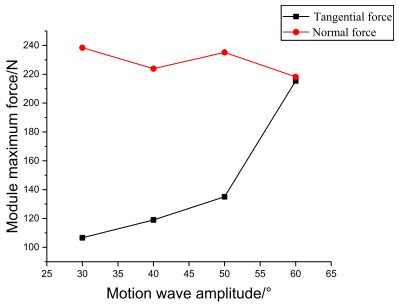

FIGURE 19. Average maximum force on the serpentine robot at each kinematic wave amplitude.

The dataset obtained by varying the kinematic wave amplitude was processed to obtain the average maximum force on the serpentine robot at each kinematic wave amplitude, as shown in Fig. 19.

The motions of the serpentine robot were simulated in a lunar crater environment with a specific kinematic wave model. Approximately 40,000 sets of data were processed to obtain the force diagram and maximum force of each module in every scenario. The forces were divided into tangential forces and normal forces, which are responsible for driving and steering the robot, respectively. The effects associated with the randomness of lunar soil distributions were also considered during the simulation. The maximum forces on the robot were analyzed to define the extreme limits of the forces that the robot must withstand, whereas the average forces on the serpentine robot were used to optimize the locomotion strategy of the robot. Among the three aforementioned parameters (crater-wall inclination, crawling angle, and kinematic wave amplitude), it was observed that the inclination of the crater wall has the smallest effect on the motions of the robot, and the effects associated with the crawling angle and kinematic wave amplitude are much larger by comparison. More specifically, the normal forces that steer the robot are most significantly affected by the crawling angle, and the tangential forces that drive the robot forward are most significantly affected by the amplitude of the robot's kinematic wave. Hence, in a lunar crater, the movements of the serpentine robot are much more strongly affected by the lunar soil environment than the mass of the robot.

V. EXPERIMENTAL VALIDATION OF THE LOCOMOTIVE FORCE OF THE SERPENTINE ROBOT

After establishing the dependencies of serpentine robot on the three aforementioned parameters, we then created an underdriven serpentine robot model and used an experimental surface environment to validate the findings of the simulation analysis. We chose to validate experimentally the effects of crawling angle and kinematic wave amplitude, which were observed to affect the serpentine robot significantly in the simulation analysis. Three values were selected for each of these parameters: the kinematic wave amplitude was varied among 30°, 40°, and 60° whereas the crawling angle was

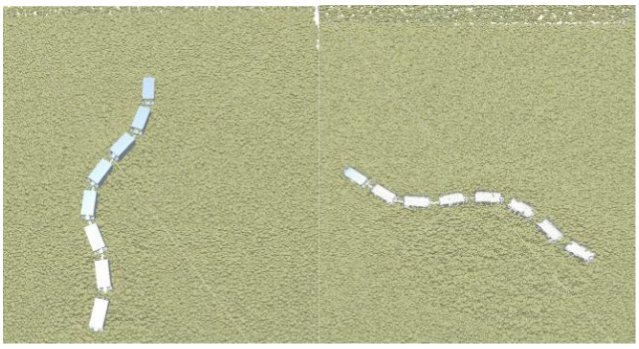

FIGURE 20. Schematic diagram of the simulated lunar surface environment.

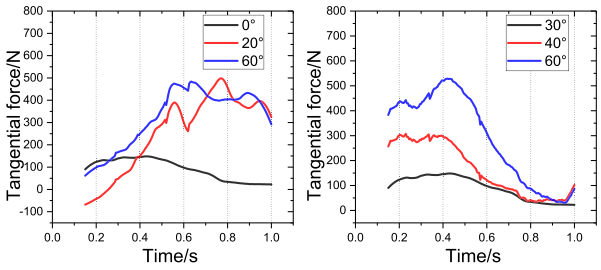

a) Tangential force at different crawling angles
b) Tangential force at different kinematic wave amplitudes

FIGURE 21. Dependence of the overall tangential force of the serpentine robot on the crawling angle and kinematic wave amplitude in the simulated lunar surface environment.

TABLE 7. Experimental results obtained with various crawling angles.

Crawling angle	Overall driving force/N
0°	91.23
20°	258.09
60°	324.59

varied among 0°, 20°, and 60°. A schematic diagram of this simulation is shown in Fig. 20

In this figure, it is shown that an increase in gravitational acceleration increased the number of tumbling lunar soil particles. During the data analysis, we only recorded the tangential force variations of the serpentine robot. The dependence of the overall tangential force of the robot on the crawling angle and kinematic wave amplitude is shown in Fig. 21.

By processing the data in this figure, we obtained the average force on the robot at all instants, as shown in Tables 7 and 8.

The driving force of the serpentine robot at different crawling angles was measured using the method illustrated in Fig. 22. In the first set of experiments, the dependence of the driving force on the kinematic wave amplitude was measured with a crawling angle of 0°. The dependence of the

TABLE 8. Experimental results obtained with various kinematic wave amplitudes.

Kinematic wave amplitude	Overall driving force/N
0°	91.23
20°	165.07
60°	292.37

FIGURE 22. Experiments with differentcrawling angles.

driving force on the crawling angle was obtained by increasing the crawling angle in the other two sets of experiments. When the crawling angle was large, the traction provided by the counterweight at the front of the robot was insufficient for the serpentine robot to move up the inclined plane. Therefore, a leash was added to the center of the robot, and counterweights were added to either end of the robot until it could move up the inclined plane. The masses of the counterweights at this point were then recorded.

Three measurements were averaged in each experiment, and the crawling angle of the serpentine robot was gradually increased in successive experiments. The mass of the balancing counterweights (480 g) was subtracted from the results to obtain the counterweight masses that represent the required driving force for the serpentine robot to crawl up the inclined plane, as shown in Table 9.

TABLE 9. Experiments with different crawling angles.

	0°	30°	60°
Counterweight mass in the first run/g	1120	1210	1270
Counterweight mass in the second run/g	1035	1190	1260
Counterweight mass in the third run/g	1175	1160	1350
Average mass/N	11.1	11.87	12.93
Driving force/N	6.30	7.17	8.13

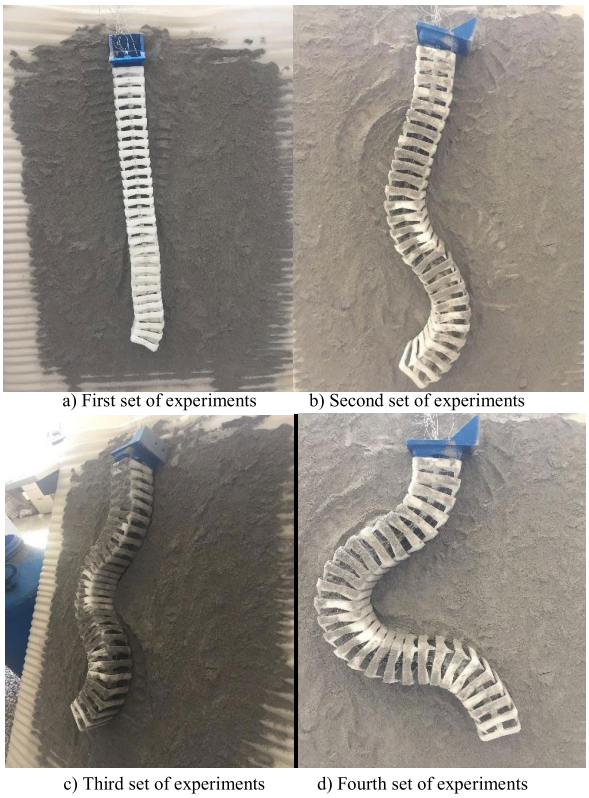

FIGURE 23. Schematic diagrams of the experiments performed with different kinematic wave amplitudes.

TABLE 10. Experiments with different kinematic wave amplitudes.

	First set	Second set	Third set	Fourth
Counterweight mass in the first run/g	965	1060	1120	1245
Counterweight mass in the second run/g	965	1085	1035	1210
Counterweight mass in the third run/g	965	1060	1175	1160
Average mass/N	9.65	10.68	11.1	12.05
Driving force/N	4.85	5.88	6.30	7.25

The counterweight mass required to move the serpentine robot was then measured with different kinematic wave amplitudes. First, a certain number of counterweights were added to the front of the serpentine robot to balance the robot on the inclined plane; the mass of these weights was 480 g. Schematic diagrams that describe the experiments with different kinematic wave amplitudes are shown in Fig. 23.

Three measurements were averaged in each experiment. The first measurement was performed on a serpentine robot without a kinematic wave, and the amplitude of the kinematic wave was gradually increased in successive experiments. The weight of the balancing counterweights (480 g) was subtracted from the results to obtain the counterweight mass

that represents the magnitude of the driving force required by the serpentine robot to crawl up the inclined plane, as shown in Table 10.

In the above experiments, it is shown that increasing the kinematic wave amplitude and crawling angle of the serpentine robot makes it easier for the robot to stay on an inclined surface. Although the effects of crawling angle on the driving force were somewhat more pronounced in the experiment than in the theoretical analysis, the conclusions derived from the simulation analysis are, as a whole, consistent with those derived from the experiment.

VI. CONCLUSION

In this study, we investigated the motional characteristics of serpentine robots suitable for probing the walls of lunar craters. The structure of the serpentine robot was designed according to the characteristics of snakes, and we constructed a kinematic model for the serpentine robot that accounts for the lunar crater environment and the sinkage of the serpentine robot in this environment. The overall structure of the serpentine robot was simplified, and various lunar soil discrete particle models were constructed. The kinematic wave model was then employed on a co-simulation platform to analyze the motional characteristics of the serpentine robot. Thus, we analyzed the effects of the crater-wall's angle of inclination, and the robot's crawling angle and kinematic wave amplitude on the forces acting on the serpentine robot. Finally, experiments were conducted to validate the findings derived from the kinematic wave model and simulation analysis. The results of this study will serve as a useful reference for lunar crater explorations in the future.

REFERENCES

[1] P. G. Lucey, D. T. Blewett, and B. R. Hawke, "Mapping the FeO and TiO_2 content of the lunar surface with multispectral imagery," *J. Geophys. Res.*, vol. 103, no. E2, pp. 3679–3699, Feb. 1998.

[2] D. J. Lawrence, W. C. Feldman, B. L. Barraclough, A. B. Binder, R. C. Elphic, S. Maurice, M. C. Miller, and T. H. Prettyman, "Thorium abundances on the lunar surface," *J. Geophys. Res.*, vol. 105, no. E8, pp. 20307–20331, Aug. 2000.

[3] P. Lucey, "Understanding the lunar surface and space-moon interactions," *Rev. Mineral. Geochem.*, vol. 60, no. 1, pp. 83–219, Jan. 2006.

[4] R. P. Lin, "Lunar surface magnetic fields and their interaction with the solar wind: Results from lunar prospector," *Science*, vol. 281, no. 5382, pp. 1480–1484, Sep. 1998.

[5] R. L. Korotev, B. L. Jolliff, R. A. Zeigler, J. J. Gillis, and L. A. Haskin, "Feldspathic lunar meteorites and their implications for compositional remote sensing of the lunar surface and the composition of the lunar crust," *Geochimica et Cosmochimica Acta*, vol. 67, no. 24, pp. 4895–4923, Dec. 2003.

[6] I. Tanev, T. Ray, and A. Buller, "Automated evolutionary design, robustness, and adaptation of sidewinding locomotion of a simulated snake-like robot," *IEEE Trans. Robot.*, vol. 21, no. 4, pp. 632–645, Aug. 2005.

[7] C. Wright, A. Johnson, A. Peck, Z. Mccord, A. Naaktgeboren, P. Gianfortoni, M. Gonzalez-Rivero, R. Hatton, and H. Choset, "Design of a modular snake robot," in *Proc. IEEE/RSJ Int. Conf. Intell. Robots Syst.*, Oct. 2007, pp. 2609–2614.

[8] J. W. Burdick, J. Radford, and G. S. Chirikjian, "A 'sidewinding' locomotion gait for hyper-redundant robots," *Adv. Robot.*, vol. 9, no. 3, pp. 195–216, 1995.

[9] T. Zhang and D. I. Goldman, "The effectiveness of resistive force theory in granular locomotion," *Phys. Fluids*, vol. 26, no. 10, Oct. 2014, Art. no. 101308.

[10] I. Tanev and K. Shimohara, "Co-evolution of active sensing and locomotion gaits of simulated snake-like robot," in *Proc. 10th Annu. Conf. Genetic Evol. Comput. (GECCO)*, 2008, pp. 257–264.

[11] S. S. Sharpe, S. A. Koehler, R. M. Kuckuk, M. Serrano, P. A. Vela, J. Mendelson, and D. I. Goldman, "Locomotor benefits of being a slender and slick sand-swimmer," *J. Exp. Biol.*, vol. 218, no. 7, p. 1111, Apr. 2015.

[12] B. C. Jayne and M. W. Daggy, "The effects of temperature on the burial performance and axial motor pattern of the sand-swimming of the Mojave fringe-toed lizard Uma scoparia." *J. Exp. Biol.*, vol. 203, pp. 1241–1252, Apr. 2000.

[13] R. A. How and R. Shine, "Ecological traits and conservation biology of five fossorial 'sand-swimming' snake species (Simoselaps: Elapidae) in south-western Australia," *Proc. Zoolog. Soc. London*, vol. 249, no. 3, pp. 269–282, 2010.

[14] C.-C. Lan, J.-H. Wang, and C.-H. Fan, "Optimal design of rotary manipulators using shape memory alloy wire actuated flexures," *Sens. Actuators A, Phys.*, vol. 153, no. 2, pp. 258–266, Aug. 2009.

[15] K. Wang, W. Gao, and S. Ma, "Snake-like robot with fusion gait for high environmental adaptability: Design, modeling, and experiment," *Appl. Sci.*, vol. 7, no. 11, p. 1133, Nov. 2017.

[16] C. Gong, D. I. Goldman, and H. Choset, "Simplifying gait design via shape basis optimization," *Robot., Sci. Syst.*, 2016.

[17] F. Kasahara, T. Yanagida, and K. Onodera, "Modeling and locomotion control using SDRE of snake-like robot considering side-slip," *Trans. Jpn. Soc. Simul. Technol.*, vol. 10, vol. 1, pp. 35–45, 2018.

[18] S. Xiao, Z. Bing, K. Huang, and Y. Huang, "Snake-like robot climbs inside different pipes," in *Proc. IEEE Int. Conf. Robot. Biomimetics (ROBIO)*, Dec. 2017, pp. 1232–1239.

[19] D. I. Hembree and S. T. Hasiotis, "Biogenic structures produced by sand-swimming snakes: A modern analog for interpreting continental ichnofossils," *J. Sedimentary Res.*, vol. 77, no. 5, pp. 389–397, May 2007.

[20] J. Xiao and X. Chen, "Buckling morphology of an elastic beam between two parallel lateral constraints: Implication for a snake crawling between walls," *J. Roy. Soc. Interface*, vol. 10, no. 85, Aug. 2013, Art. no. 20130399.

[21] K. Dowling, "Limbless locomotion: Learning to crawl," in *Proc. IEEE Int. Conf. Robot. Autom.*, vol. 4, Jan. 2003, pp. 3001–3006.

[22] P. Prautsch and T. Mita, "Control and analysis of the gait of snake robots," in *Proc. IEEE Int. Conf. Control Appl.*, vol. 1, Aug. 1999, pp. 502–507.

[23] M. Tesch, J. Schneider, and H. Choset, "Using response surfaces and expected improvement to optimize snake robot gait parameters," in *Proc. IEEE/RSJ Int. Conf. Intell. Robots Syst.*, Sep. 2011, pp. 1069–1074.

[24] S. Hasanzadeh and A. A. Tootoonchi, "Ground adaptive and optimized locomotion of snake robot moving with a novel gait," *Auton. Robot*, vol. 28, no. 4, pp. 457–470, May 2010.

[25] C. Gong, M. J. Travers, H. C. Astley, L. Li, J. R. Mendelson, D. I. Goldman, and H. Choset, "Kinematic gait synthesis for snake robots," *Int. J. Robot. Res.*, vol. 35, nos. 1–3, pp. 100–113, Jan. 2016.

[26] D. Ruffatto, A. Parness, and M. Spenko, "Improving controllable adhesion on both rough and smooth surfaces with a hybrid electrostatic/gecko-like adhesive," *J. Roy. Soc. Interface*, vol. 11, no. 93, Apr. 2014, Art. no. 20131089.

[27] T. L. Lam and Y. Xu, "Motion planning for tree climbing with inchworm-like robots," *J. Field Robot.*, vol. 30, no. 1, pp. 87–101, Jan. 2013.

[28] M. Tavakoli, L. Marques, and A. T. De Almeida, "3DCLIMBER: Climbing and manipulation over 3D structures," *Mechatronics*, vol. 21, no. 1, pp. 48–62, Feb. 2011.

[29] H. Zhu, Y. Guan, W. Wu, X. Chen, X. Zhou, and H. Zhang, "A binary approximating method for graspable region determination of biped climbing robots," *Adv. Robot.*, vol. 28, no. 21, pp. 1405–1418, Nov. 2014.

[30] M. Tavakoli, P. Lopes, L. Sgrigna, and C. Viegas, "Motion control of an omnidirectional climbing robot based on dead reckoning method," *Mechatronics*, vol. 30, pp. 94–106, Sep. 2015.